

Confining single Er^{3+} ions in sub-3 nm NaYF_4 nanoparticles to induce slow relaxation of the magnetisation

Received: 26 August 2022

Accepted: 9 April 2024

Published online: 25 April 2024

Check for updates

Diogo A. Gálico¹, Emille M. Rodrigues¹, Ilias Halimi¹, Juho Toivola², He Zhao³, Jiahui Xu³, Jani O. Moilanen²✉, Xiaogang Liu³, Eva Hemmer^{1,4}✉ & Muralee Murugesu^{1,4}✉

Molecular systems known as single-molecule magnets (SMMs) exhibit magnet-like behaviour of slow relaxation of the magnetisation and magnetic hysteresis and have potential application in high-density memory storage or quantum computing. Often, their intrinsic magnetic properties are plagued by low-energy molecular vibrations that lead to phonon-induced relaxation processes, however, there is no straightforward synthetic approach for molecular systems that would lead to a small amount of low-energy vibrations and low phonon density of states at the spin-resonance energies. In this work, we apply knowledge accumulated over the last decade in molecular magnetism to nanoparticles, incorporating Er^{3+} ions in an ultrasmall sub-3 nm diamagnetic NaYF_4 nanoparticle (NP) and probing the slow relaxation dynamics intrinsic to the Er^{3+} ion. Furthermore, by increasing the doping concentration, we also investigate the role of intraparticle interactions within the NP. The knowledge gained from this study is anticipated to enable better design of magnetically high-performance molecular and bulk magnets for a wide variety of applications, such as molecular electronics.

Magnetic materials are ubiquitous in our daily lives, ranging from electric motors, cars and turbines to electronic devices, and their need is projected to increase exponentially in the future as we approach decarbonization¹. Therefore, it is critical to develop lighter, stronger, and higher-performing magnetic materials. The magnet-like behavior of traditional bulk magnets often originates from the intimate interconnection and collective behavior of each individual spin center. To understand the overall macroscopic behavior of a magnet (e.g., slow magnetic relaxation dynamics), it is important to examine the basic units of bulk material at the atomic level, and shed light on the intrinsic properties of individual components (e.g., spin state of metal ions). Improved understanding of the unique role of these components at the atomic level makes it possible to tune and optimize their bulk

physicochemical properties, as well as to develop high-performing materials. For instance, in permanent magnets such as $\text{Nd}_2\text{Fe}_{14}\text{B}$ and $\text{Sm}_2\text{Co}_{17}$ alloys, the incorporation of rare-earth (RE) ions provides significant magnetic anisotropy, leading to large magnetic coercivity and thus, magnetic hardness^{2–6}. However, elucidating the exact contribution of each component at the atomic level remains a challenge.

As molecular model systems can provide insight into the spin and magnetic anisotropy, RE-based molecular systems, namely single-molecule magnets (SMMs), have been intensively developed over the past two decades^{7–9}. Some of these systems exhibit magnet-like behavior of slow relaxation of the magnetization below their blocking temperature (T_B ; below which, the material acts like a magnet), and giant coercivity that at times surpasses the coercive fields of

¹Department of Chemistry and Biomolecular Sciences, University of Ottawa, Ottawa, ON K1N 6N5, Canada. ²Department of Chemistry, Nanoscience Centre, University of Jyväskylä, P.O. Box 35, FI-40014 Jyväskylä, Finland. ³Department of Chemistry, National University of Singapore, 3 Science Drive 3, Singapore 117543, Singapore. ⁴Centre for Advanced Materials Research (CAMaR), University of Ottawa, Ottawa, ON K1N 6N5, Canada. ✉e-mail: jani.o.moilanen@jyu.fi; ehemmer@uottawa.ca; M.Murugesu@uottawa.ca

permanent magnets^{7–9}. Mononuclear dysprosocenium complexes that act as SMMs above liquid nitrogen's temperature demonstrated remarkable magnetic performance can arise from a single RE center^{10,11}. Although molecular systems can provide insight into the spin and magnetic anisotropy, the bulky ligands used to achieve a low coordination environment induce a high-density of molecular vibrations over a broad spectral range (from hundreds to a few thousand wavenumbers)^{12,13}. The high-density of (low-energy) molecular vibrations increases the probability of the phonons coupling with (low-energy) electronic states, resulting in phonon-assisted relaxation which reduces the energy barrier (U_{eff}) and the overall magnetic performance of a system. Currently, the upper limit for relaxation barriers with existing compounds have already been reached¹⁴. Therefore, to further minimize phonon-assisted relaxation and improve the overall magnetic performance of a molecular magnet, it is critical to incorporate magnetic ions in a host matrix that not only provide a low vibrational density of states at the spin resonance energies but also rigidity at the molecular level that leads to a small amount of low-energy vibrations that can couple with low-energy (acoustic) phonons¹⁵.

In contrast, nanoparticles (NPs), based on inorganic elements, provide an alternative ionic framework for the RE ions in which vibrational modes are in more discrete frequency ranges than in molecular compounds (see ESI for details)^{16–27}. They also exhibit distinct vibrational modes, whose positions and intensities can be modulated by the nature of doped RE ions.

Additionally, their set crystalline lattice offers well-defined local high symmetry around metal centers, thus enabling symmetry consideration, a unique aspect in this study. Thus, NPs can be seen as interesting alternative host materials to investigate single-ion magnet (SIM) behavior at the atomic level with and without neighboring magnetic centers. The gained knowledge will be leveraged to gain a better understanding of classical bulk magnets and consequently lay the basis for the development of better performing bulk magnets. Small nanoparticles contain several hundreds of atoms which renders atomic-level analysis difficult. Thus, in an attempt to isolate one paramagnetic ion in a diamagnetic NP host, ultrasmall sub-3 nm NPs are targeted. Owing to their high chemical reactivity and behavior similarities, RE ions can be chemically “interchangeable” at the atomic level with their congeners within the crystalline lattice. This has been the method of choice for enhancing and harnessing luminescent properties in mixed-metal RE-based NPs (RE-NPs)^{28,29}. In addition, low dopant concentrations allow for efficient dilution of RE³⁺ ions at the atomic level. Recent achievements in the chemical synthesis of small and ultrasmall RE-NPs offer an excellent level of RE-ion/host tunability, being leveraged, for instance, into upconverting and near-infrared (NIR) emitting RE-NPs^{30–32}. RE-NPs, such as alkali metal RE fluorides (MREF₄, e.g., M = Na, Li, K; RE = Y, Gd) doped with upconverting or near-infrared emitting RE³⁺ dopant ions (e.g., Er/Yb, Tm/Yb, Nd, Ho and their combinations) have made strides in the field of novel upconverting and NIR-emitting nanoparticles^{28–32}.

To shed light on the magnetic contribution of individual components to bulk materials, we have focused on isolating a paramagnetic RE³⁺ ion (namely Er³⁺) through doping within a diamagnetic NaYF₄ NP host. Our ultimate goal is to sequester one Er³⁺ ion *per* NP and probe its magnetic properties at the atomic level within this alternative framework for molecular compounds. Subsequently, by increasing the concentration of Er³⁺ ions within the RE-NPs, we intend to systematically investigate the role of Er-Er interactions at various dopant concentrations; i.e., the influence of close Er³⁺ ion proximity on the overall magnetic properties. As such, a slow relaxation mechanism can be probed using SQUID magnetometry at first at the individual atomic level and subsequently with the presence of neighboring paramagnetic ions by carefully controlling the percentage of dopant ions. Herein, we present the elucidation of the slow relaxation of the magnetization of

Er³⁺ at the atomic level achieved through its meticulous dilution in a NaYF₄ NP. Observed magnetic relaxation dynamics at the single-ion level within the NaYF₄ NP represents the first report of SIM behavior in a RE-based nanoparticle. The knowledge gained from this unique study could unravel the untapped potentials of RE-based nanoparticles for applications ranging from memory storage at a single-atom level to fine-tuning high-performing hard magnets in a controlled fashion, which can be used for molecular electronic applications.

Results and discussions

Ultrasmall (*ca* 2.7 nm, Fig. 1a) diamagnetic fluoride-type cubic-phase α -NaYF₄ NPs were chosen as host for Er³⁺ ions acting as the paramagnetic component by replacing the diamagnetic Y³⁺ ions in the crystalline lattice. Various Er³⁺ nominal concentrations (1, 2, 4, 6, 8, and 10 mol%—hereafter, respective samples are named NPX with X being the Er³⁺ nominal concentration) were probed to understand the role of Er-Er distances on the overall magnetic properties. Upon dilution of Er³⁺ ions in these NPs at 1% molar concentration, we anticipate only one Er³⁺ ion to be present per NP (Fig. 1b); thus, we target to probe the magnetic relaxation of the single Er³⁺ ion at the atomic level in the rigid NP host.

RE-doped NaYF₄ NPs can be isolated in cubic α - or hexagonal β -phase. The Y centers in the α -phase adopt an eight-coordinate environment, while in the β -phase, two different nine-coordinate C_{3v} sites are observed. More specifically, the α -phase of NaYF₄ can be described as CaF₂-type, with only one possible cation site of high symmetry (O_h), half occupied by Na⁺ ions and half occupied by RE³⁺ ions (Fig. 1c)²⁸. In theory, the single high symmetry cubic coordination environment provided by α -NaYF₄ should eliminate the multiple relaxation processes originating from the different site symmetries of occupied sites that could be observed for β -phase due to the two different nine-coordinate C_{3v} sites. In other words, α -phase is more straightforward to investigate than β -phase as there is only one possible high-symmetry site for cation. As previously mentioned, the main goal of this study is to prove that the knowledge obtained over the last decades with molecular compounds can be applied to nanoparticles; therefore, choosing a simpler system with an expected single-relaxation process is an exciting approach when translating the knowledge for the nanoparticle field for the first time. Although the pure O_h symmetry stabilizes the isotropic ground state that is prone to the fast relaxation of the magnetization contrast to the anisotropic ground state³³, any distortions on the O_h site can give rise to the magnetic anisotropy of Er³⁺ ions³⁴. With that said, some slight but non-negligible distortion around the RE³⁺ coordination environment is expected given the slightly different ionic radii of the dopant and host RE³⁺ ion (1.15 Å for Y³⁺ and 1.14 Å for Er³⁺)^{35,36}. Moreover, decreasing the particle size to the nanoscale leads to higher surface tensions, which can result in a stabilization of the higher symmetry for these NPs—in some cases, even large enough to lead to a phase transition from an anisotropic to a more isotropic crystalline phase³⁷. The Er³⁺-doped α -NaYF₄ NPs (NaYF₄:Er³⁺) were synthesized using the microwave-assisted thermal decomposition of RE³⁺ oleate precursors, as described in previous work³⁸, resulting in ultrasmall NPs capped with oleate (–OA) groups. Regardless of the Er³⁺ dopant concentration (1, 2, 4, 6, 8, or 10 mol%), all the synthesized NPs crystallized in the pure cubic (α)-phase of NaYF₄ (Fig. S1), exhibiting a spherical morphology of comparable sizes ranging from 2.5 to 2.7 nm (Figs. 1a, b and S2). Inductively coupled plasma (ICP) analysis (Table S1) was performed to confirm the Er³⁺ ion concentration in the synthesized NPs.

The number of Er³⁺ ions in each of the synthesized NPs was calculated as previously reported by Wilhelm and co-workers (see ESI)³⁹, indicating the presence of 1 (NP1), 2 (NP2), 4 (NP4), 7 (NP6), 9 (NP8), and 12 (NP10) Er³⁺ ions *per* NP (Table S2). To further understand the distribution of Er³⁺ ions within the NP, Monte Carlo simulations were performed (Figs. 1d, e and S4 and Table S3). For each NP composition, these simulations provided a mean Er³⁺–Er³⁺ distance within the

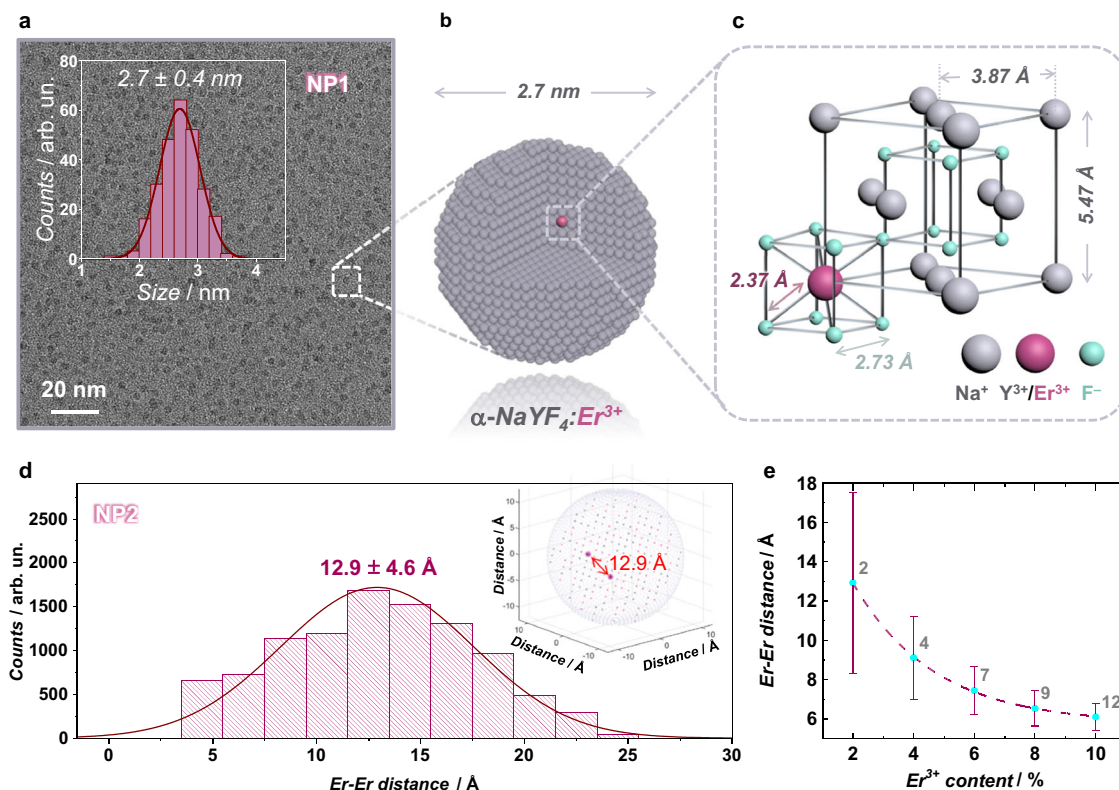


Fig. 1 | Structural analysis for the NPs. a Transmission electron microscopy (TEM) image and size distribution of α -NaYF₄ NPs doped with 1 mol% Er³⁺ (NP1).

b Schematic representation of NP1 containing one Er³⁺ ion. **c** Cubic lattice unit cell of NaYF₄ indicating the positions of Na⁺, Y³⁺, and F⁻ host ions as well as Er³⁺ dopants. The cubic lattice was adapted from ref. 14 for α -NaYF₄. **d** Er³⁺-Er³⁺ distance

distribution for NP2 calculated with Monte Carlo model (inset: Monte Carlo model of the number of Er³⁺ ions and the mean Er³⁺-Er³⁺ distance for NP2). **e** Mean Er³⁺-Er³⁺ distance for the NPs as a function of the Er³⁺ content. Gray labels indicate the number of Er³⁺ ions within the NP as determined by ICP analysis. TEM images and Er³⁺-Er³⁺ distance distributions for all other compositions are given at the ESI.

diamagnetic host. For instance, for NP2 containing two Er³⁺ ions *per* NP, the mean distance between the two Er³⁺ ions was determined as 12.9 Å. Increasing the number of Er³⁺ ions *per* NP resulted in the decrease of the mean distance, hence, approximation of the paramagnetic Er³⁺ ions and yielding the shortest distance of 6.1 Å for NP10 (12 Er³⁺ ions *per* NP).

To probe the intrinsic magnetic properties of the Er³⁺ ions isolated within the α -NaYF₄ host and how the intraparticle dipolar interactions could affect the slow relaxation of the magnetization, we have carried out in-depth direct current (dc) and alternating current (ac) magnetic susceptibility measurements on NPs with different Er³⁺ doping concentrations. It is important to notice that thermogravimetric (TGA) analysis of the NPs (Fig. S3) confirmed a similar amount of residual hexane and oleate ligands at the surface of the NPs, allowing for normalization in relation to the mass for the magnetic data. Dc measurements are shown in Fig. 2a as mass susceptibility ($\chi_g T$) *vs.* temperature (T) from 300 K down to 1.8 K. For all the doping concentrations, an almost constant $\chi_g T$ value was observed from room temperature down to -100 K. The decrease of the $\chi_g T$ values below this temperature is likely due to depopulation of the ligand field sublevels as often encountered in RE systems^{40,41}. More importantly, for NP1, NP2, and NP4, $\chi_g T$ values at 1.8 K (Fig. 2c) increase linearly according to the anticipated number of Er³⁺ ions *per* particle. This trend is indicative of negligible magnetic interactions between paramagnetic metal centers within the particles as the intraparticle Er³⁺-Er³⁺ distance is predicted to be above 9 Å for NP 2 and NP4, based on Monte Carlo simulations (Table S3). Whereas, increasing the Er³⁺ concentration (above 6 mol%) resulted in a deviation from this linearity, thus, suggesting an increase in intraparticle dipolar magnetic interactions due to the greater amount of Er³⁺ ions within the NPs and hence shorter Er³⁺-Er³⁺ distances. To further understand our observation, $\chi_g T$ *vs.* T was also

collected with a field of 1T (Fig. 2b, d). As can be noted, with a higher field, linearity at 1.8 K occurs up to NP8. Correlating the dc magnetic data with the mean Er³⁺-Er³⁺ distances within each NP (Fig. 1e) suggests that a distance close to and below 8 Å is the critical distance to increase the intraparticle dipolar interactions. The finding is supported by the calculated dipolar coupling parameters decrease with the increasing Er³⁺-Er³⁺ distance (r): $J_{\text{dip}} = -1.07 \text{ cm}^{-1}$ ($r = 3.868 \text{ Å}$), $J_{\text{dip}} = -0.38$ ($r = 5.470 \text{ Å}$), $J_{\text{dip}} = -0.09$ ($r = 8.649 \text{ Å}$), and $J_{\text{dip}} = -0.05$ ($r = 10.940 \text{ Å}$). It is evident from the calculated data that the strength of the dipolar coupling at -8 Å is one order of magnitude smaller than at -3 Å. Because the dipolar interaction is inverse proportional to the third power of the distance between the magnetic centers, its magnitude and influence on the magnetic properties of magnetic sites decreases with increasing distance as proven by the data obtained for the studied NPs and previously reported SMMS⁴²⁻⁴⁵. Furthermore, this intraparticle dipolar interaction is anticipated to affect on the quantum tunneling of the magnetization (QTM) and relaxation times (ac data, *vide infra*).

To probe the magnet-like behavior of slow relaxation of the magnetization originating from a single Er³⁺ ion level, ac susceptibility studies in the 0.1–1500 Hz range were performed with an oscillating field of $H_{\text{ac}} = 3.78 \text{ Oe}$. In the absence of an applied static dc magnetic field, ac susceptibility signals were not observed. Such behavior is common for RE ions as they are prone to undergo QTM^{46,47}. To minimize QTM and visualize slow relaxation of the magnetization, a static dc field can be applied. As such, to elucidate the optimal applied dc field, field-dependent relaxation dynamics were investigated at 1.9 K for each Er³⁺ concentration (Fig. 3 left).

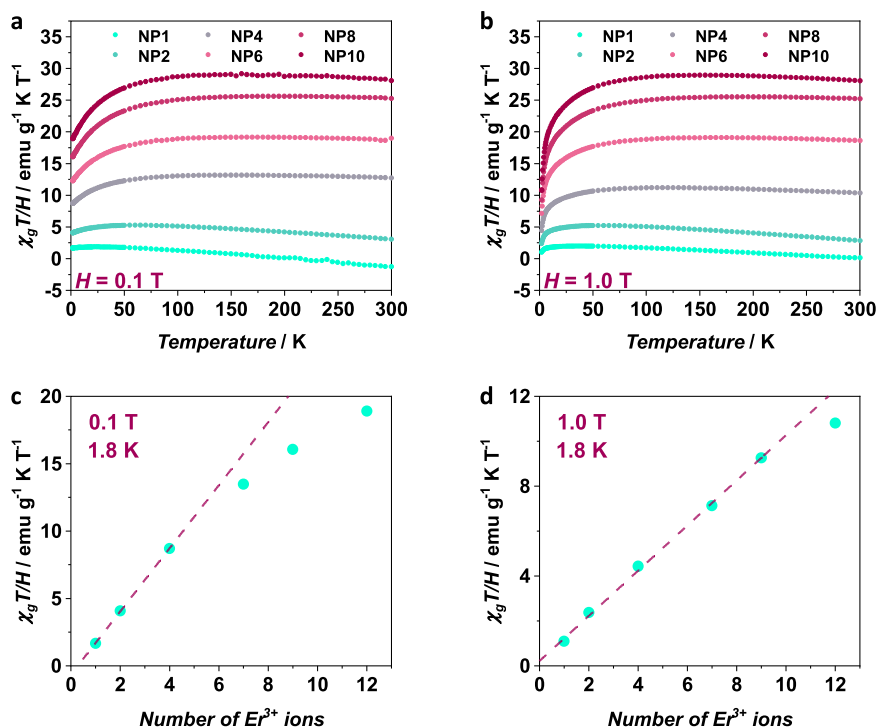


Fig. 2 | Direct current (dc) magnetic susceptibility measurements for the NPs. a Mass susceptibility ($\chi_g T/H$) as a function of temperature with an applied field of 0.1 T and **(b)** 1 T. **c** The number of Er³⁺ ions dependence of the $\chi_g T/H$ value at 1.8 K with an applied field of 0.1 T and **(d)** 1 T. Source data are provided as a Source Data file.

Frequency-dependent signals in the out-of-phase χ'' susceptibility were observed between 100–5000 Oe (and 400–5000 Oe for NP10), yielding a bimodal profile and indicating the presence of slow magnetic relaxation. Of these two frequency-dependent peak maxima, one is dominant at the high-frequency region (≥ 100 Hz; denoted as process 1) and the other at the low-frequency region (≤ 10 Hz; process 2) and both are inversely related to the applied field strength. For NP6, NP8, and NP10, most of the high-frequency process 1 occurs outside the experimental range (>1500 Hz). Notable, process 1 is shifted for lower frequencies when decreasing the number of Er³⁺ ions within the NP host, evidencing the impact of the paramagnetic ion isolation in decreasing the relaxation rate^{48–52}.

The field-dependent τ (relaxation time) values were obtained from the fit of the χ'' susceptibility to the generalized double Debye model to consider both processes⁵³. It should be noted the large distribution of τ values expressed as large α values (Tables S4–S9). The estimated standard deviations (ESD) of the relaxation time have been calculated from the α -parameter of the generalized Debye fits and the log-normal distribution as previously described⁵⁴. This large distribution may occur due to inherent nature of ultrasmall nanoparticles in which the large surface/volume ratio results in a significant number of ions located close to the surface and possessing a higher degree of distortion. Upon careful inspection of τ values, it is evident that process 2 (for NP1–NP10) is predominately QTM (Fig. S5 and Table S10). Whereas for NP1–NP4, the τ values for the high-frequency process 1 were fit to Eq. (1), which includes the Raman, the field-dependent direct and tunneling mechanisms (Fig. S6 and Table S10):

$$\tau^{-1} = AH^4 + CT^n + \frac{B_1}{(1 + B_2 H^2)} \quad (1)$$

The best-fit parameters are summarized in Table S10. For process 1, the relaxation dynamics observed for $H_{dc} \leq 1000$ Oe are attributed to QTM, whereas when $H_{dc} \geq 2000$ Oe, the direct mechanism takes over as the predominant pathway. It should be noted that for process 1, QTM B_1 parameter values increase from NP1 to NP4. For process 1

QTM, it is not possible to unequivocally determine if the nature of the process is due to intraparticle, interparticle, or a combination of both. For example, in NP4 the mean distance between the Er³⁺ ions was determined as 9.1 Å, while for NP2 the mean distance between the two Er³⁺ ions was determined as 12.9 Å. If we assume two NP1 aggregated side-by-side (see TEM image, Fig. 1a), containing only one Er³⁺ ion, and with the Er³⁺ ion perfectly positioned in the center of the NP, the distance between these Er³⁺ ions will be 26.9 Å. If the ions at two neighboring NPs are not located in the center but facing each other, the distance between the Er³⁺ ions can be even smaller. At these distances, the presence of the process 1 QTM can be expected, and the lower B_1 value, when compared to NP2 and NP4, is in agreement with the increased distancing. Additionally, the observation of intraparticle-mediated QTM for NP1 cannot be fully ruled out. Although our data and calculations suggest the presence of only one Er³⁺ per NP for NP1, NPs are not perfectly homogeneous in terms of composition, thus one can expect that a small but non-negligible amount of NPs contains more than one Er³⁺ ion within the structure. Hence, unequivocally assignment of the process 1 QTM is not possible since both intra- and interparticle interactions can be reasonably explained based on the NP structural features. From this data, the optimal field to ensure minimal contributions from each of these mechanisms is 1800 Oe. At this field, the τ reaches the maximum values of 1.83, 0.74, 0.19 ms, and for NP1, NP2, and NP4, respectively. Such trends demonstrate that relaxation time at the atomic level for Er³⁺ ion is highly influenced by the presence of nearest Er³⁺ neighbors. Reducing the dopant concentration from 4 to 1 mol% (i.e., 4 Er³⁺ ions per NP to one Er³⁺ ion per NP), the large distribution of τ values became one order of magnitude slower at the optimal field (1800 Oe). This data suggests that SIM-like behavior attributed to Er³⁺ ions can be attained at atomic level within a rigid NP matrix.

A closer inspection of low-frequency process 2 dynamics indicates an interparticle nature for this process because the QTM is present even at higher fields. Such behavior was previously observed for the [Co_xZn_{1-x}(DAPBH)(NO₃)(H₂O)](NO₃) molecular system⁵⁵. Furthermore, QTM relaxation rates for process 2 are in full agreement with dc data;

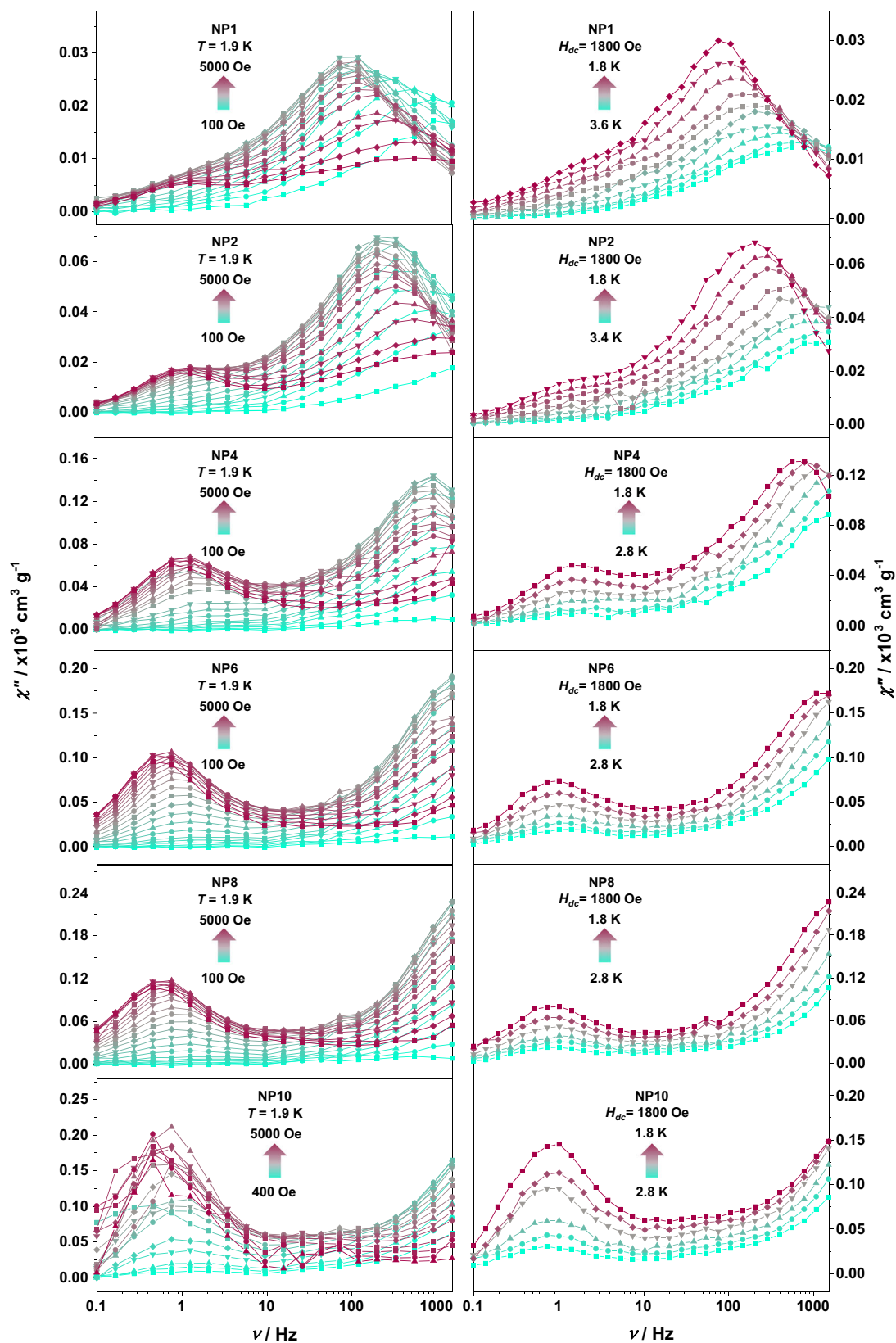


Fig. 3 | Dynamic magnetic susceptibility data for the NPs. Frequency dependence of the out-of-phase (χ'') magnetic susceptibility for NP1 to NP10 (from top to bottom) obtained at 1.9 K as a function of the applied magnetic field (left) and

under an applied static field of 1800 Oe as a function of temperature (right). Source data are provided as a Source Data file.

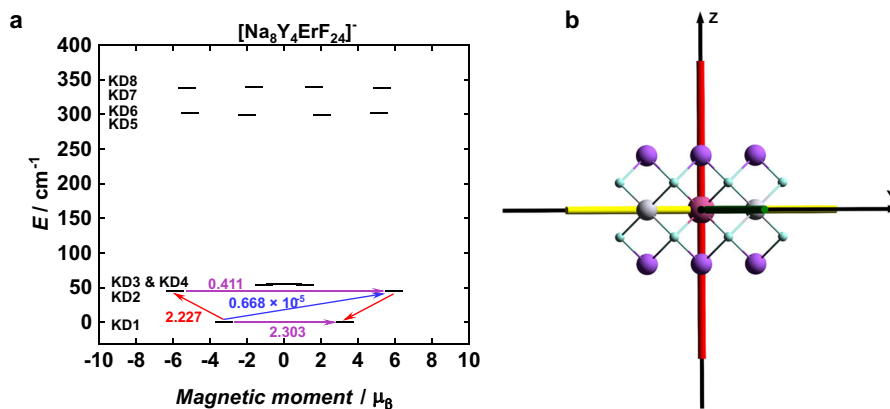


Fig. 4 | Crystal field sublevels and magnetic axis for the $[\text{Na}_8\text{Y}_4\text{ErF}_{24}]^-$ theoretical model. a Energy spectra and qualitative magnetization blocking barriers for $[\text{Na}_8\text{Y}_4\text{ErF}_{24}]^-$. Black lines represent the calculated Kramers doublets, and they are placed in the spectrum according to their magnetic moment. The numbers show the transition probabilities (in μ_B) between the calculated Kramers doublets

for the two lowest-lying spin-orbit states. Red, blue and purple lines correspond to direct, Orbach, and QTM processes, respectively. **b** Orientation of the main magnetic axes $-X_m$ (green), Y_m (yellow) and Z_m (red) of the ground Kramers doublet of Er^{3+} ion in $[\text{Na}_8\text{Y}_4\text{ErF}_{24}]^-$ fragment. See Fig. S9 for additional information and a comparison with other fragments.

for NP1, NP2, and NP4, B_1 values were above 10 s^{-1} while for NP6, NP8, and NP10, the values decreased to below 10 s^{-1} , in agreement with the linearity deviation shown at Fig. 2b. This is in agreement with the expectations since not only intraparticle interactions are affected when more Er^{3+} ions are confined within a single NP, but also the probability of interparticle interaction increases.

In order to further compare and probe the magnetic performance of the NPs, temperature-dependent relaxation dynamics were investigated under an external applied field of 1800 Oe (Fig. 3 right). Frequency-dependent out-of-phase (χ'') susceptibilities were observed at low temperature, exhibiting magnet-like behavior, indicative of slow relaxation of the magnetization. As for the field-dependent relaxation dynamic, a bimodal profile was observed with similar behavior. The temperature-dependent τ values were obtained from the fit of the χ'' susceptibility to the generalized double Debye model. As for the field-dependent data, process 2 is due to QTM originated by the interparticle dipolar interactions (Fig. S7 and Table S17). The τ values for process 1 were fit to Eq. (2):

$$\tau^{-1} = CT^n + \tau_{\text{QTM}}^{-1} \quad (2)$$

The best-fit parameters are summarized in Table S17. For NP4, NP2, and NP1, the Raman process alone is enough to reproduce the experimental data successfully. However, the relaxation rates became one order of magnitude slower when comparing NP4 and NP1 ($\tau_{1.8\text{K}}^{-1} = 3952$ and 478 s^{-1} for NP4 and NP1, respectively). Such observation further affirms that a single Er^{3+} ion confined within the NP matrix can act as a single-ion magnet. Attempts to obtain hysteresis measurements revealed no retention of the magnetic moment at 1.8 K for all the synthesized NPs, presumably due to the small energy barrier observed.

To investigate the microscopic magnetic properties of the synthesized NPs in detail, we carried out the CASSCF/SO-RASSI calculations for six different NP fragments— $[\text{Na}_8\text{Y}_4\text{ErF}_{22}]^+$, $[\text{Na}_8\text{Y}_4\text{ErF}_{23}]$, $[\text{Na}_8\text{Y}_4\text{ErF}_{24}]^-$, $[\text{Na}_8\text{Y}_{10}\text{ErF}_{40}]^+$, $[\text{Na}_8\text{Y}_{10}\text{ErF}_{41}]$, and $[\text{Na}_8\text{Y}_{10}\text{ErF}_{42}]^-$ —with varying size, charge, and symmetry (see ESI for details). Comparison of the computational data to previously published results^{56–58}, particularly, to the EPR study of 8 nm cubic $\text{NaY}_{0.98}\text{Er}_{0.02}\text{F}_4$ nanoparticles⁵⁶, revealed that the $[\text{Na}_8\text{Y}_4\text{ErF}_{24}]^-$ fragment with D_{4h} symmetry simulates the C.F. around the Er^{3+} ion very well. Thus, only the results obtained for $[\text{Na}_8\text{Y}_4\text{ErF}_{24}]^-$ are discussed in detail (Fig. 4). Furthermore, to get insight on the phonon spectra of the investigated NPs, the periodic boundary conditions DFT (pDFT) calculations were carried out for a-

phase of NaYF_4 and $\text{NaY}^{167,259}\text{F}_4$ of which the latter simulates the effects of Er^{3+} ions on the phonon properties (see ESI for details).

An investigation of the weights of M_j components reveals that the ground Kramers doublet (KD) of the $[\text{Na}_8\text{Y}_4\text{ErF}_{24}]^-$ fragment is composed of the $M_j = \pm 13/2$, $\pm 5/2$, $\pm 3/2$, and $\pm 11/2$ states, that is expected for the system in which Er^{3+} ion occupies the O_h site symmetry (Table S27; see ESI for details)⁵⁷. The compositions of the excited KDs are also in line with the previously reported values for the Ln^{3+} ions residing in the cubic environment and they indicate that the excited KDs cannot be either assigned to any pure M_j states due to the pseudo O_h site symmetry of the Er^{3+} ion in the $[\text{Na}_8\text{Y}_4\text{ErF}_{24}]^-$ fragment strongly mix the different M_j states³⁴. As evident from the g -tensor ($g_x = 6.91$, $g_y = 6.91$, $g_z = 6.57$) of the ground KD of $[\text{Na}_8\text{Y}_4\text{ErF}_{24}]^-$, the calculations predict almost completely isotropic ground state for Er^{3+} ions with the average g -value of 6.79 that is in excellent agreement with the g -value of 6.80 obtained from the EPR study of cubic $\text{NaY}_{0.98}\text{Er}_{0.02}\text{F}_4$ nanoparticle⁵⁶ (Table S24). Such a low axiality facilitates the QTM within the ground KD effectively, as proven by the calculated transition probability (Fig. 4). These results readily explain the fast relaxation of the magnetization of NPs without an applied dc field. If the QTM within the ground KD could be suppressed with the applied dc field, it is highly unlikely that the Orbach process *via* the low-lying first-excited KD (44.8 cm^{-1}), as depicted in Fig. 4, would take place because the first excited KD has a larger magnetization than the isotropic ground KD. The result further supports the experimental findings that slow relaxation of magnetization originates from the Raman process and QTM in the studied NPs under an applied dc field. Interestingly, the DFT calculations reveal that the first optical phonon modes for NaYF_4 and $\text{NaY}^{167,259}\text{F}_4$ are at 125 cm^{-1} and 122 cm^{-1} , respectively (Figs. S12 and S13). Given that the thermal population of optical phonon modes will be minimal in the low temperature region ($< 3.6 \text{ K}$), where NPs show slow relaxation of magnetization, it is more likely that acoustic phonons mediate the relaxation processes of the studied NPs. Optical phonons usually couple stronger to the spins than acoustic ones, but in the low temperature region the role of acoustic phonons cannot be ruled out⁵⁹. In sharp contrast to molecular compounds, for which a high density of dispersive pseudoacoustic/low energy optical phonon modes are observed even below 20 cm^{-1} , these modes are absent in NaYF_4 and $\text{NaY}^{167,259}\text{F}_4$ (Figs. S12 and S13)^{15,60}. As proposed by Lunghi et al., the high frequency value of the first optical phonon mode of the crystal cell, as observed for NaYF_4 and $\text{NaY}^{167,259}\text{F}_4$, could be taken as one of the design strategies to ensure the small amount of

low-energy vibrations in the lattice, low phonon density of states at the spin resonance energies, and rigidity of ligands to minimize the coupling of intramolecular motions to low-energy acoustic phonons¹⁵. Indeed, NaYF₄ and NaY^{167,259}F₄ have a small amount of low-energy vibrations (Fig. S10 and Tables S21 and S20) and the energies of the first four KDs of the [Na₈Y₄ErF₂₄]⁻ fragment are in the region (0–54 cm⁻¹) where the phonon density of states is small (Table S24 and Figs. S12 and S13). Despite these facts, low-energy acoustic phonons most likely couple to the spins of Er³⁺ centers because slow relaxation of magnetization of the investigated NPs takes place in the temperature region where only the thermal population of acoustic phonons is significant, and the energies of the higher lying KDs (KD5–KD8) are in an energy range of 300–350 cm⁻¹ of optical phonons with a high density of states. The former can be partly explained by the fact that a large part of phonon distributions originates from F and Er atoms in the low-energy region of acoustic phonons, as shown by the projected density of states (Fig. S13). While the phonon density of states does not always correlate with the spin-phonon coupling intensities¹⁵, the above qualitative analysis shows that the NaYF₄ NPs can function as host materials that partly obey the current design principles for the high-performing SIMs.

The calculated C.F. parameters (B_{kq}) show an interesting trend for [Na₈Y₄ErF₂₄]⁻. The B₄₀ and B₆₀ diagonal parameters contribute significantly to the C.F. However, the off-diagonal parameters B₄₄, and B₆₄ also substantially contribute to reducing the overall axiality of the fragment (Table S33). All other C.F. parameters are essentially zero for [Na₈Y₄ErF₂₄]⁻. These features originate from the O_h site symmetry of the doped NPs. Thus, the CASSCF/SO-RASSI calculations do not only indicate the modest SIM behavior of investigated Er³⁺-doped NPs, but they also highlight that SIM based on NPs doped at low concentration can strictly follow the symmetry design criteria of SMM⁶¹. This is a significant finding because it is not easy to synthesize the molecular system that would possess an exact high symmetry coordination environment around Ln³⁺ ion obeying the symmetry design criteria rigorously. However, ideal local O_h symmetry around the RE³⁺ ion will automatically lead to a system in which the ground KD is completely isotropic, like in [Na₈Y₄ErF₂₄]⁻ (Table S24), and prone to strong QTM³². Thus, future synthetic efforts should focus on doped NPs in which the high crystal symmetry is accompanied by a high local symmetry other than O_h symmetry. For example⁶², in doped fluorites, the Er³⁺ ions can form a hexameric cluster with F⁻ ions in which the Er³⁺ ions occupy the D_{4d} site symmetry that is known to stabilize the axial ground KD ($g_x \approx g_y \approx 0.00$, $g_z \approx 18.00$) with almost pure $M_J \pm 15/2$ state in case of Er³⁺ ions³⁴.

In summary, by applying the knowledge accumulated over the last decade in the molecular field, we successfully demonstrated that slow magnetic relaxation could be attained for a single Er³⁺ ion within a nanoparticle matrix. This was achieved by implementing doping into a rigid diamagnetic α -NaYF₄ NP matrix. Upon dilution at 1 mol% concentration, it is possible to isolate a single paramagnetic Er³⁺ ion that sits in a cubic coordination environment (O_h symmetry) in these ultrasmall sub-3 nm NPs. At this low concentration, Er³⁺-Er³⁺ interactions were minimized, which resulted in slower relaxation rates when compared with NPs containing more than one Er³⁺ ion. Although the relaxation process occurs *via* Raman and QTM processes in the low temperature region where acoustic phonons dominate the phonon spectra, this study proves that this methodology can be extended to NPs with greater crystal symmetry and rigid framework with further enhanced SMM behavior. The employed concentration dependant study further demonstrates that interatomic distances can be controlled to correlate various relaxation mechanisms promoted due to proximity between paramagnetic centers. We envision such studies can ultimately enable careful and selective doping of traditional magnets and other magnetic materials to isolate the next generation of ultra-hard magnets.

Methods

Nanoparticle synthesis

Yttrium oxide (Y₂O₃, 99.99%) and erbium oxide (Er₂O₃, 99.99%) were purchased from Alfa Aesar. Oleic acid (CH₃(CH₂)₇CHCH(CH₂)₇COOH, OA, 90%), oleylamine (CH₃(CH₂)₇CHCH(CH₂)₇CH₂NH₂, OAm, 70%), 1-octadecene (ODE, 90%), and ammonium fluoride (NH₄F, 98%) were purchased from Sigma-Aldrich. Sodium oleate (CH₃(CH₂)₇CHCH(CH₂)₇COONa, Na-OA, 97%) was purchased from Tokyo Chemical Industry. Toluene (99.8%) was purchased from Fisher Scientific. Ethanol (99%) and hexane (analytical grade) were purchased from Commercial Alcohols and Fisher Chemicals, respectively. All chemicals were used as received.

Cubic-phase Er³⁺-doped NaYF₄ nanoparticles were synthesized using the microwave-assisted thermal decomposition of RE³⁺ oleate precursors ([RE(OA)₃], OA: CH₃(CH₂)₇CH=CH(CH₂)₇COO⁻), as previously reported²⁸. [RE(OA)₃] precursors were prepared following an adopted procedure reported in the literature⁶³. In brief, 0.625 mmol of RECl₃·6H₂O (RE = Y³⁺ and Er³⁺—the relative amounts of chlorides for each NP composition are given in Table S1), 3.75 mmol (1141.7 mg) of sodium oleate (Na-OA), and a mixture of 2.8 ml of water, 3.8 ml of ethanol, and 6.6 ml of hexane were added to a 50 ml round-bottom flask. The flask was fitted to a condenser and the mixture was refluxed under vigorous stirring for 2 h at 70 °C. Subsequently, the organic layer containing [RE(OA)₃] was washed three times with 4 ml of a 1:1 water-to-ethanol mixture in a separatory funnel. Ten ml of 1-octadecene (ODE) was added to the [RE(OA)₃] solution in hexane and the residual solvent was evaporated at 70 °C under a gentle flow of N₂ for 20 min. For the synthesis of α -NaYF₄:Er³⁺ NPs (Er³⁺ dopant concentration X = 1, 2, 4, 6, 8 or 10 mol%), 1.15 mmol (380.55 mg) of Na-OA and 10 ml of oleic acid were added to the [RE(OA)₃]-ODE mixture (resulting in a 1:1 Na⁺-to-RE³⁺ molar ratio), and the solution was degassed under vacuum at 100 °C for 30 min. A 10 ml aliquot of this reaction mixture was transferred into a 35 ml microwave vessel containing 2.5 mmol (94.5 mg) of NH₄F, purged with N₂, tightly sealed, inserted into a CEM Discover SP microwave, and subjected to the following reaction profile: (1) medium stirring at room temperature for 1 min and rapid heating to 100 °C (1 min) under slow stirring, (2) slow stirring with rapid increase in temperature to 240 °C (5 min), (3) rapid cooling to 230 °C (15 s), (4) static heating at 230 °C (10 min) under slow stirring, and (5) gradual cooling to 50 °C (6 min). Following the synthesis, the reaction mixture containing the NPs was transferred into a centrifugation tube, diluted with a 1:3 hexane-to-ethanol mixture and centrifuged at 6595 × g for 20 min. The product was then washed with a 1:3 toluene-to-acetone mixture and centrifuged using the same conditions reported above. After purification, the NPs were dispersed and stored in 5 ml hexane for further use.

Samples for TGA and SQUID measurements were dried overnight in a Schlenk line.

Characterizations and methods

To determine the crystal phase of the NPs, powder X-ray diffraction (XRD) analysis was performed using a Rigaku Ultima IV Diffractometer (Cu K α , $\lambda = 1.5401 \text{ \AA}$), operating at 44 kV and 40 mA (step size: 0.02°, scan speed: 0.7° min⁻¹). The size and morphology of the NPs were determined by transmission electron microscopy (TEM) using a FEI Tecnai Spirit microscope operating at 120 kV. The samples were diluted in hexane from the original stock suspensions by 50 times and 6 μ l of the diluted suspension was dropped on a Formvar/carbon film supported by a 300-mesh copper TEM grid. Thermogravimetric analysis (TGA) of the NPs was carried out using a TGA Q500/Discovery under N₂ atmosphere and at a heating rate of 10 °C min⁻¹.

The Er³⁺ dopant concentration in each of the NPs compositions was determined by inductively coupled plasma–optical spectrometry (ICP-OES) using an Agilent ICP-OES spectrometer (nebulizer flow of 0.71 min⁻¹, plasma flow 12 l min⁻¹, auxiliary flow 1 l min⁻¹). The samples

were prepared by digesting 10 μl of the NP stock suspensions in hexane with 0.5 ml of HNO_3 and 1.5 ml of HCl at 40 $^\circ\text{C}$ overnight, followed by the dilution with distilled water to 5 ml.

The magnetic susceptibility measurements were obtained using a Quantum Design SQUID magnetometer MPMS-XL7 operating between 1.8 and 300 K. Direct (dc) and/or alternate (ac) current measurements were performed on dried samples restrained with silicon grease and wrapped in a polyethylene membrane. The samples were subjected to dc fields of -7 to 7T, and a 3.78 Oe driving field was used for ac measurements. The magnetization data were collected at 100 K to check for ferromagnetic impurities that were absent in all samples. Diamagnetic corrections were applied for the sample holder and the inherent diamagnetism of the samples were estimated with the use of Pascals constants.

Data availability

All data obtained and analyzed are present in the manuscript and the Supplementary Material. The raw data for Figs. 2 and 3 are made available as source data. All the other raw data that support the findings of this study are available from the corresponding authors upon request. Source data are provided with this paper.

References

- Bobba, S. et al. *Critical Raw Materials for Strategic Technologies and Sectors in the EU—A Foresight Study* (European Commission, 2020).
- Tanaka, S. et al. First principles study on the local magnetic anisotropy near surfaces of $\text{Dy}_2\text{Fe}_{14}\text{B}$ and $\text{Nd}_2\text{Fe}_{14}\text{B}$ magnets. *J. Appl. Phys.* **109**, 07A802 (2011).
- Boltich, E. B. & Wallace, W. E. Differences in the low temperature magnetic anisotropy of $\text{Nd}_2\text{Fe}_{14}\text{B}$ and $\text{Pr}_2\text{Fe}_{14}\text{B}$ interpreted on a crystal field model. *Solid State Commun.* **55**, 529–532 (1985).
- Yehia, S. & Aly, S. H. J. Magnetic anisotropy and spin reorientation in $\text{Nd}_2\text{Fe}_{14}\text{B}$. *Magn. Mater.* **212**, 195–200 (2000).
- Télliez-Blanco, J. C., Kou, X. C. & Grössinger, R. Coercivity and magnetic anisotropy of sintered $\text{Sm}_2\text{Co}_{17}$ -type permanent magnets. *J. Appl. Phys.* **82**, 3928 (1997).
- Szpunar, B. & Lindgard, P. A. On the origin of the large magnetic anisotropy of rare Earth-cobalt compounds. *J. Phys. F Met. Phys.* **9**, L55 (1979).
- Coronado, E. Molecular magnetism: from chemical design to spin control in molecules, materials and devices. *Nat. Rev. Mater.* **5**, 87–104 (2020).
- Marin, R., Brunet, G. & Murugesu, M. Shining new light on multifunctional lanthanide single-molecule magnets. *Angew. Chem. Int. Ed.* **60**, 1728–1746 (2021).
- Mavragani, N. et al. Radical-bridged Ln_4 metallocene complexes with strong magnetic coupling and a large coercive field. *Angew. Chem. Int. Ed.* **60**, 24206–24213 (2021).
- Goodwin, C. A. P., Ortu, F., Reta, D., Chilton, N. F. & Mills, D. P. Molecular magnetic hysteresis at 60 Kelvin in dysprosocenium. *Nature* **548**, 439–442 (2017).
- Guo, F.-S. et al. Magnetic hysteresis up to 80 kelvin in a dysprosium metallocene single-molecule magnet. *Science* **362**, 1400–1403 (2018).
- Lunghi, A., Totti, F., Sessoli, R. & Sanvito, S. The role of anharmonic phonons in under-barrier spin relaxation of single molecule magnets. *Nat. Commun.* **8**, 14620 (2017).
- Evans, P., Reta, D., Whitehead, G. F. S., Chilton, N. F. & Mills, D. P. Bis-monophospholyl dysprosium cation showing magnetic hysteresis at 48 K. *J. Am. Chem. Soc.* **141**, 19935–19940 (2019).
- Reta, D., Kragoskow, J. G. C. & Chilton, N. F. Ab initio prediction of high-temperature magnetic relaxation rates in single-molecule magnets. *J. Am. Chem. Soc.* **143**, 5943–5950 (2021).
- Briganti, M. et al. A complete ab initio view of Orbach and Raman spin-lattice relaxation in a dysprosium coordination compound. *J. Am. Chem. Soc.* **143**, 13633–13645 (2021).
- Suyver, J. F. et al. Upconversion spectroscopy and properties of NaYF_4 doped with Er^{3+} , Tm^{3+} and/or Yb^{3+} . *J. Lumin.* **117**, 1–12 (2006).
- Zhang, Z. et al. Tuning phonon energies in lanthanide-doped potassium lead halide nanocrystals for enhanced nonlinearity and upconversion. *Angew. Chem. Int. Ed.* **62**, e202212549 (2023).
- Dubey, C. et al. Impact of crystal structure on optical properties and temperature sensing behavior of $\text{NaYF}_4:\text{Yb}^{3+}/\text{Er}^{3+}$ nanoparticles. *RSC Adv.* **13**, 20975–20983 (2023).
- Assaaoudi, H., Shan, G.-B., Dyck, N. & Demopoulos, G. P. Annealing-induced ultra-efficient NIR-to-VIS upconversion of nano-/micro-scale α and β $\text{NaYF}_4:\text{Er}^{3+}, \text{Yb}^{3+}$ crystals. *CrystEngComm* **15**, 4739–4746 (2013).
- Yang, D. et al. Controllable phase transformation and mid-infrared emission from Er^{3+} -doped hexagonal-/cubic- NaYF_4 nanocrystals. *Sci. Rep.* **6**, 29871 (2016).
- Wang, Z., Li, X., Zhang, G., Luo, Y. & Jiang, J. Suppressing electron-phonon coupling through laser-induced phase transition. *ACS Appl. Mater. Interfaces* **9**, 23309–23313 (2017).
- Thokwane, P. & Mbule, P. Analysis of the $\text{NaYF}_4:\text{Yb}^{3+}, \text{Er}^{3+}$ nanocrystals: up-conversion luminescence, crystal structure and morphology influenced by the dopant concentration and annealing temperature. *Bull. Mater. Sci.* **46**, 140 (2023).
- Wang, G. et al. Controlled synthesis and luminescence properties from cubic to hexagonal $\text{NaYF}_4:\text{Ln}^{3+}$ ($\text{Ln} = \text{Eu}$ and Yb/Tm) microcrystals. *J. Alloy. Compd.* **475**, 452–455 (2009).
- Renner-Lecuna, C. et al. Origin of the high upconversion green luminescence efficiency in β - $\text{NaYF}_4:2\%\text{Er}^{3+}, 20\%\text{Yb}^{3+}$. *Chem. Mater.* **23**, 3442–3448 (2011).
- Chen, Q., Li, Z., Miao, B. & Ma, Q. Thermal, nonlinear, magnetic and faraday rotation properties of sol-gel diamagnetic glass/ $\text{NaYF}_4:\text{Fe}, \text{Ho}^{3+}$: Role of magnetic ions. *J. Alloy. Compd.* **858**, 157631 (2021).
- Tuyen, V. T. et al. Controllable structural and optical properties of $\text{NaYF}_4:\text{Tm}, \text{Yb}$ microparticles by Yb^{3+} doping for anti-counterfeiting. *RSC Adv.* **13**, 19317–19324 (2023).
- Luo, X. & Akimoto, K. Upconversion properties in hexagonal-phase $\text{NaYF}_4:\text{Er}^{3+}/\text{NaYF}_4$ nanocrystals by off-resonant excitation. *Appl. Surf. Sci.* **273**, 257–260 (2013).
- Wang, F. et al. Simultaneous phase and size control of upconversion nanocrystals through lanthanide doping. *Nature* **463**, 1061–1065 (2010).
- Wang, F. et al. Tuning upconversion through energy migration in core-shell nanoparticles. *Nat. Mater.* **10**, 968–973 (2011).
- Li, H., Wang, X., Ohulchanskyy, T. Y. & Chen, G. Lanthanide-doped near-infrared nanoparticles for biophotonics. *Adv. Mater.* **33**, 2000678 (2021).
- Wilhelm, S. Perspectives for upconverting nanoparticles. *ACS Nano* **11**, 10644–10653 (2017).
- Wu, Y., Ang, M. J. Y., Sun, M., Huang, B. & Liu, X. Expanding the toolbox for lanthanide-doped upconversion nanocrystals. *J. Phys. D Appl. Phys.* **52**, 383002 (2019).
- Liu, J.-L. et al. Switching the anisotropy barrier of a single-ion magnet by symmetry change from quasi- D_{5h} to quasi- O_h . *Chem. Sci.* **4**, 3310–3316 (2013).
- Baldovi, J. J. et al. Rational design of single-ion magnets and spin qubits based on mononuclear lanthanoid complexes. *Inorg. Chem.* **51**, 12565–12574 (2012).
- Tu, D. et al. Breakdown of crystallographic site symmetry in lanthanide-doped NaYF_4 crystals. *Angew. Chem. Int. Ed.* **52**, 1128–1133 (2013).

36. Shannon, R. D. & Prewitt, C. T. Effective ionic radii in oxides and fluorides. *Acta Crystallogr. B Struct. Cryst. Cryst. Chem.* **25**, 925–946 (1969).
37. Ayyub, P., Palkar, V. R., Chattopadhyay, S. & Multani, M. Effect of crystal size reduction on lattice symmetry and cooperative properties. *Phys. Rev. B* **51**, 6135–6138 (1995).
38. Halimi, I. et al. Pick your precursor! Tailoring the size and crystal phase of microwave-synthesized sub-10 nm upconverting nanoparticles. *J. Mater. Chem. C* **7**, 15364–15374 (2019).
39. Wilhelm, S. et al. Water dispersible upconverting nanoparticles: effects of surface modification on their luminescence and colloidal stability. *Nanoscale* **7**, 1403–1410 (2015).
40. Sessoli, R. & Powell, A. K. Strategies towards single molecule magnets based on lanthanide ions. *Coord. Chem. Rev.* **253**, 2328–2341 (2009).
41. Zhu, Z., Guo, M., Li, X.-L. & Tang, J. Molecular magnetism of lanthanide: advances and perspectives. *Coord. Chem. Rev.* **378**, 350–364 (2019).
42. Le Roy, J. J. et al. Coupling strategies to enhance single-molecule magnet properties of erbium–cyclooctatetraenyl complexes. *J. Am. Chem. Soc.* **136**, 8003–8010 (2014).
43. Gálico, D. A. et al. Triplet-state position and crystal-field tuning in opto-magnetic lanthanide complexes: two sides of the same coin. *Chem. Eur. J.* **25**, 14625–14637 (2019).
44. Kitos, A. A. et al. Probing optical and magnetic properties via subtle stereoelectronic effects in mononuclear Dy^{III}-complexes. *Chem. Comm.* **57**, 7818–7821 (2021).
45. Huang, G. et al. Magnetic slow relaxation in a metal–organic framework made of chains of ferromagnetically coupled single-molecule magnets. *Chem. Eur. J.* **24**, 6983–6991 (2018).
46. Ishikawa, N., Sugita, M. & Wernsdorfer, W. Nuclear spin driven quantum tunneling of magnetisation in a new lanthanide single-molecule magnet: Bis(phthalocyaninato)holmium anion. *J. Am. Chem. Soc.* **127**, 3650–3651 (2005).
47. Ishikawa, N., Sugita, M. & Wernsdorfer, W. Quantum tunneling of magnetisation in lanthanide single-molecule magnets: Bis(phthalocyaninato)terbium and Bis(phthalocyaninato)dysprosium anions. *Angew. Chem. Int. Ed.* **44**, 2931–2935 (2005).
48. Dong, H.-M., Li, H. Y., Zhang, Y.-Q., Yang, E. C. & Zhao, X.-J. Magnetic relaxation dynamics of a centrosymmetric Dy₂ single-molecule magnet triggered by magnetic-site dilution and external magnetic field. *Inorg. Chem.* **56**, 5611–5622 (2017).
49. Meihaus, K. R., Rinehart, J. D. & Long, J. R. Dilution-induced slow magnetic relaxation and anomalous hysteresis in trigonal prismatic dysprosium(III) and uranium(III) complexes. *Inorg. Chem.* **50**, 8484–8489 (2011).
50. Hu, Z.-B. et al. Optimal diamagnetic dilution concentration for suppressing the dipole–dipole interaction in single-ion magnets. *Dalton Trans.* **49**, 2159–2167 (2020).
51. Wang, M. et al. Impact of ligand substituents on the magnetization dynamics of mononuclear Dy^{III} single-molecule magnets. *Inorg. Chem.* **61**, 9785–9791 (2022).
52. Nehr Korn, J. et al. Easy-plane to easy-axis anisotropy switching in a Co(II) single-ion magnet triggered by the diamagnetic lattice. *J. Mater. Chem. C* **9**, 9446–9452 (2021).
53. Li, J. et al. Two field-induced slow magnetic relaxation processes in a mononuclear Co(II) complex with a distorted octahedral geometry. *Dalton Trans.* **45**, 9279–9284 (2016).
54. Reta, D. & Chilton, N. F. Uncertainty estimates for magnetic relaxation times and magnetic relaxation parameters. *Phys. Chem. Chem. Phys.* **21**, 23567–23575 (2019).
55. Habib, F., Korobkov, I. & Murugesu, M. Exposing the intermolecular nature of the second relaxation pathway in a mononuclear cobalt(II) single-molecule magnet with positive anisotropy. *Dalton Trans.* **44**, 6368–6373 (2015).
56. García-Flores, A. F. et al. Crystal-field Stark effect on the upconversion light emission spectrum of α-NaYF₄ nanoparticles doped with Dy³⁺, Er³⁺, or Yb³⁺. *Phys. Rev. B* **106**, 125427 (2022).
57. Lea, K. R., Leask, M. J. M. & Wolf, W. P. The raising of angular momentum degeneracy of f-Electron terms by cubic crystal fields. *J. Phys. Chem. Solids* **23**, 1381–1405 (1962).
58. Dantelle, G., Mortier, M. & Vivien, D. EPR and optical studies of erbium-doped β-PbF₂ single-crystals and nanocrystals in transparent glass–ceramics. *Phys. Chem. Chem. Phys.* **9**, 5591–5598 (2007).
59. Gu, L. & Wu, R. Origins of slow magnetic relaxation in single-molecule magnets. *Phys. Rev. Lett.* **125**, 117203 (2020).
60. Nabi, R. et al. Accurate and efficient spin-phonon coupling and spin dynamics calculations for molecular solids. *J. Am. Chem. Soc.* **145**, 24558–24567 (2023).
61. Liu, J.-L., Chen, Y.-C. & Tong, M.-L. Symmetry strategies for high performance lanthanide-based single-molecule magnets. *Chem. Soc. Rev.* **47**, 2431–2453 (2018).
62. Nikiforov, A. E. et al. Crystal fields of hexameric rare-Earth clusters in fluorites. *Phys. Solid State* **47**, 1431–1435 (2005).
63. Kang, N., Ai, C.-C., Zhou, Y.-M., Wang, Z. & Ren, L. Facile synthesis of upconversion nanoparticles with high purity using lanthanide oleate compounds. *Nanotechnology* **29**, 075601 (2018).

Acknowledgements

D.A.G. and M.M. thank the University of Ottawa, the CFI, the Natural Sciences and Engineering Research Council of Canada for financial support of this work. E.H., E.M.R. and I.H. gratefully acknowledge the financial support provided by the University of Ottawa and the Natural Sciences and Engineering Research Council of Canada (NSERC, RGPIN-2016-04830). J.T. and J.O.M. acknowledge the Research council of Finland (projects 315829, 345484, and 338733) for the financial support, and Prof. Heikki M. Tuononen (University of Jyväskylä) for providing computational resources for the project. We also thank Prof. Antti Karttunen for the useful discussion related to the periodic boundary density functional theory calculations.

Author contributions

D.A.G., E.H. and M.M. conceived the study. I.H., E.M.R. and E.H. synthesized and characterized the nanoparticles. D.A.G. collected and interpreted the magnetic data. H.Z., J.X. and X.L. performed Monte Carlo simulations and analysis. J.T. and J.O.M. performed theoretical calculations and analysis. M.M. supervised all aspects of the project. The manuscript was written with contributions from all authors.

Competing interests

The authors declare no competing interests.

Additional information

Supplementary information The online version contains supplementary material available at <https://doi.org/10.1038/s41467-024-47682-x>.

Correspondence and requests for materials should be addressed to Jani O. Moilanen, Eva Hemmer or Muralee Murugesu.

Peer review information *Nature Communications* thanks Nicholas Chilton, and the other, anonymous, reviewer(s) for their contribution to the peer review of this work. A peer review file is available.

Reprints and permissions information is available at <http://www.nature.com/reprints>

Publisher's note Springer Nature remains neutral with regard to jurisdictional claims in published maps and institutional affiliations.

Open Access This article is licensed under a Creative Commons Attribution 4.0 International License, which permits use, sharing, adaptation, distribution and reproduction in any medium or format, as long as you give appropriate credit to the original author(s) and the source, provide a link to the Creative Commons licence, and indicate if changes were made. The images or other third party material in this article are included in the article's Creative Commons licence, unless indicated otherwise in a credit line to the material. If material is not included in the article's Creative Commons licence and your intended use is not permitted by statutory regulation or exceeds the permitted use, you will need to obtain permission directly from the copyright holder. To view a copy of this licence, visit <http://creativecommons.org/licenses/by/4.0/>.

© The Author(s) 2024